

Nitrogen-doped carbon as selectively permeable layer to enhance the anti-poisoning ability of hydrogen oxidation reaction catalysts for hydroxide exchange membrane fuel cells

Xingdong Wang^a, Jinjie Fang^a, Xuerui Liu^a, Dong Wei^a, Yiquan Yin^a, Hailong Wei^a, Jinlin Zhang^a, Yufeng Zhang^a, Xuejiang Zhang^a, Wei Zhu^a, Zhongbin Zhuang^{a,b,*}

^a State Key Lab of Organic-Inorganic Composites and Beijing Advanced Innovation Center for Soft Matter Science and Engineering, Beijing University of Chemical Technology, China

^b Beijing Key Laboratory of Energy Environmental Catalysis, Beijing University of Chemical Technology, China



ARTICLE INFO

Keywords:

Fuel cells
Nickel
Hydrogen oxidation reaction
Anti-poisoning
Nitrogen-doped carbon

ABSTRACT

The use of platinum group metals (PGMs) as the catalysts and the requirement of high purity H₂ are the two aspects resulting in the high cost of the polymer electrolyte membrane fuel cells. Herein, we report that nitrogen-doped carbon encapsulated nickel nanoparticles (Ni@NC) as stable hydrogen oxidation reaction catalysts, which allows the use of PGM-free anode catalysts durably and feeding crude hydrogen. The hydroxide exchange membrane fuel cell using Ni@NC as the anode catalyst illustrates steady performance for more than 200 h, while the Ni/C cell fails within 7 h. The current density loss is less than 10% by feeding H₂ with 100 ppm of CO for 24 h, which is much better than those using Pt/C or Ni/C. The anti-poisoning feature is attributed to the block effect of the NC shell, while the defects allow the permeation of H₂, thus catalyzing the hydrogen oxidation reaction.

1. Introduction

The earth's increasingly rapid economic globalization and urbanization have spurred a transformation and renovation of the energy consumption structure [1]. The hydrogen economy, which constitutes H₂ production, H₂ transportation, and H₂ conversion to electricity, provides a sustainable solution and thus brought about widespread attention [2]. In the process of H₂ utilization, fuel cell technology predominates because of its high H₂ utilization efficiency and environmentally friendly emission [3]. However, the high cost of the fuel cells hindered their wide applications. The high cost of the fuel cells comes from two respects: one is the high cost of the ultrapure H₂ fuels leading to high operation cost and the other is the high cost from the fuel cell stacks leading to high capital cost.

Ultrapure H₂ is required for the polymer electrolyte membrane fuel cells, including the recently developed hydroxide exchange membrane fuel cells (HEMFCs), due to the intense poisoning effect of the impurities, such as CO, to the anode hydrogen oxidation reaction (HOR) catalysts [4,5]. The purification process significantly increased the cost of H₂ fuels. For example, crude H₂ from steam reforming costs only ~US

\$1.5 kg⁻¹. However, after removing the CO content to an acceptable level for fuel cells, the cost of H₂ increased tenfold to ~US\$13–16 kg⁻¹ [6]. Apart from CO, impurities such as H₂S, halide, hydrocarbon, etc., are often present in crude H₂ [7–10], and these substances can irreversibly damage the catalysts and worsen the fuel cell performance [11]. To prevent this situation, international standards (Table S1) were introduced to limit the concentrations of various impurities in H₂ for fuel cell vehicles (FCVs), which obviously pose extra challenges in cost reduction [12]. Therefore, utilizing the crude H₂ by using an anti-poisoning electrode is of high commercial value. However, the anode catalyst with satisfied anti-poisoning ability, particularly in a cell stack, has seldom been reported [6,11,13,14]. Another possible route to increase the anti-poisoning ability is to physically block the poisoner by capping the catalyst with a protection layer [15]. However, this layer must selectively permeate the reactant molecules/ions, otherwise the catalysts can not work. How to create a such selectively permeable protection layer is still challenging.

On the other hand, the requirement of the platinum-group metals (PGMs) for the polymer electrolyte membrane fuel cells is one of the main reasons for the high cost of the fuel cell stacks. The HEMFCs, which

* Corresponding author at: State Key Lab of Organic-Inorganic Composites and Beijing Advanced Innovation Center for Soft Matter Science and Engineering, Beijing University of Chemical Technology, China.

E-mail address: zhuangzb@mail.buct.edu.cn (Z. Zhuang).

can meet the high-power-density requirement like proton exchange membrane fuel cells, are important and promising energy conversion technology [16–19]. HEMFCs have shown the possibility of employing low-cost PGM-free cathode, bipolar plates and non-fluorinated membranes [20–23]. However, the required high PGM loadings on the anode side significantly increase the cost of the HEMFCs [24–26]. Thus, the non-precious metal-based anode HOR catalyst is critical for the development of HEMFCs [27,28]. Ni-based catalysts showed notable HOR performance in alkaline [29–33]. Recently, the activity of Ni-based catalysts has been promoted by engineering the composition and structure of the catalysts [34–37]. However, the Ni-based HOR catalysts suffered from durability issues. Apart from the poisoning effect from the impurities in the H₂, the Ni-based catalysts themselves are easier to be oxidized and thus fail for HOR [38]. Davydova et al. observed the degradation of Ni-based catalysts in alkaline electrolytes [39]. To prevent the oxidation of the catalysts, Hu's group transported their synthesized Ni catalysts and manufactured electrodes in a glove box [31]. Speck et al. reported the protection of the HOR catalysts by covering semipermeable thin CeO_x film to against oxidation and dissolution [40]. The oxidation of the Ni-based catalysts may occur during the fabrication process of the MEAs. Although some high-performance Ni-based HOR catalysts have been reported, seldom high-performance MEA have been reported. Some effects have been adopted to enhance the stability of the Ni based HOR catalysts [41,42]; however, the stability issue is still the primary problem to be resolved.

The anti-CO poisoning ability of the Ni-based HOR catalysts has gained much attention, in order to achieve low catalyst cost and low hydrogen cost simultaneously. CO strongly adsorbs on the Ni surface, and thus inhibits the HOR process. Weakening the adsorption of CO, which could be achieved by tuning the electronic structure of the catalysts, is a possible approach. Alloy Ni or doped Ni with heteroatom (e.g. MoNi₄ [43], Co-NiMo₄ [44], Ni_{5.2}WCu_{2.2} [45], and Ni₃N [46]), introducing vacancy [46], and inset oxygen in the Ni lattice [47], are reported to improve the CO anti-poisoning ability. The electronic structure of the Ni-based catalysts could be alternated by additional carbon shells. The carbon shell improved the antioxidation capability of Ni with optimal binding energies of OH_{ad} and H_{ad} [42], and the HEMFC employ the core-shell Ni anode showed stable discharge for 120 h at 0.7 V [41]. The CO anti-poisoning ability of the core-shell Ni catalysts was enhanced as well [48]. However, more highly stable Ni-based HOR catalysts, as well as advanced and comprehensive anti-poisoning researches are still desired in developing HEMFC.

In the current study, we report that the nitrogen-doped carbon (NC) can be used as the selective protection layer to enhance the stability and anti-poisoning ability of the Ni-based HOR catalysts. A nitrogen-doped carbon encapsulated nickel nanoparticles (denoted as Ni@NC) as the anode catalyst for HEMFCs is developed, which has prompted stability and high anti-poisoning effect for CO and other impurities that may exist in crude H₂. We find that a carbon shell can protect Ni, but block all the reactant, and thus hinders the HOR. However, the NC shells serve as a selectively permeable membrane, which blocks the poisoning molecules, but can permeate H₂ molecules. We find that the defects in the NC shells allow the H₂ molecules to transport to the Ni nanoparticle surface, which catalyzed the HOR. A 200 h of HEMFC stability is achieved by using the Ni@NC as the anode catalyst. And more importantly, the Ni@NC HEMFC can be fed by H₂ with 100 ppm of CO, with no significant decay on the HEMFC performance, while the Pt/C and Ni/C HEMFC performance reduce by more than 70%. Our study suggests a protection strategy to achieve low-cost robust fuel cell anode catalysts, which may allow the use of low-cost crude H₂.

2. Experimental section

2.1. Materials

Citric acid monohydrate (C₆H₈O₇·H₂O), urea (CH₄N₂O), nickel (II)

nitrate hexahydrate (Ni(NO₃)₂·6 H₂O), sodium borohydride (NaBH₄), potassium sulfide (K₂S), potassium thiocyanide (KSCN), hydrochloric acid (HCl), absolute ethanol and isopropanol used were of analytical grade and purchased from Sinopharm Chemical Reagent Co., Ltd, China. Potassium hydroxide (KOH) was of electronic grade and purchased from Sinopharm Chemical Reagent Co., Ltd, China. Ketjen black (ECP-600JD) and Vulcan XC-72R carbon were received from the Lion Company and Cabot Company, respectively. Ultrapure water (18.2 MΩ cm) was used in the whole experiment.

2.2. Synthesis of Ni@NC catalysts

300 mg of Ketjen black was dispersed in 15 mL of absolute ethanol and stirred to form a carbon slurry. Then, 3.566 g of Ni(NO₃)₂·6 H₂O, 2.304 g of citric acid, and 0.23 g of urea were dissolved in 2 mL of deionized water to obtain the precursor solution. Subsequently, the precursor solution was dropwise added into the carbon slurry with magnetic stirring. The obtained mixture was kept stirring for 2 h and then dried in an oven at 60 °C overnight. The obtained solid was annealed in N₂ atmosphere at 550 °C for 45 min to get the Ni@NC catalyst.

2.3. Physical characterizations

The morphologies of the catalysts were studied by TEM using JEOL JEM1230 transmission electron microscope. HRTEM and EDS mapping were performed on a JEOL JEM-2100 F transmission electron microscope. XAS data were collected at the TPS-21A beamline of the National Synchrotron Radiation Research Center (NSRRC, Hsinchu, Taiwan) using a Si (111) quick-scanning monochromator. Data were processed according to standard procedures using the Demeter software package (Version 0.9.26). The XPS was obtained on a Thermo Fisher ESCALAB 250Xi spectrometer with a monochromatic Al K α X-ray source. The XRD patterns were profiled on a Rigaku D/Max 2500 VB2 + /PC X-ray powder diffractometer using Cu K α radiation ($\lambda = 0.154$ nm), and all of the diffraction data were collected in a 20 range from 30° to 90° at a scanning rate of 10° min⁻¹. The Raman spectra were performed on the LabRAM ARAMIS with an Ar laser at a wavelength of 514 nm. The electrochemical *in-situ* ATR-SEIRAS were taken with Nicolet iS50 FT-IR spectrometer equipped with an MCT detector cooled with liquid nitrogen and PIKE VeeMAX III variable angle ATR sampling accessory. The detailed experimental procedure was shown in [Supplementary Information](#).

The TGA was performed on a Mettler Toledo TGA-DSC 3 + analyzer under air from room temperature to 800 °C with a heating rate of 5 °C min⁻¹. CO TPD was performed on an AutoSorb iQ-C-TCD analyzer and ca. 50 mg of the catalyst was loaded in a U-shape quartz reactor. The sample was pretreated at 200 °C under Ar for 1 h. After cooling down to 50 °C, the samples were saturated in 10% CO/Ar flow for 60 min, and purged with Ar for another 60 min. After that, the sample was heated to 600 °C with a heating rate of 10 °C min⁻¹ under Ar flow and the desorbed gas was monitored by a TCD detector.

2.4. Electrochemical measurements

All electrochemical performances were measured in 0.1 M KOH electrolyte controlled by an electrochemical workstation (V3, Princeton Applied Research) combined with a rotating disk electrode (RDE). A 5 mm diameter glassy carbon electrode (PINE Instruments) with a deposited catalyst layer was used as the working electrode. The catalyst layer was prepared by casting the catalyst ink on the glassy carbon electrode, which has already been polished to a mirror using 0.05 μm of Al₂O₃. The catalyst ink was prepared by dispersing 5 mg of catalyst in a solution consisting of 100 μL of H₂O, 895 μL of isopropanol, and 5 μL of Nafion solution (Du Pont, 5 wt%). The dispersion was sonicated for 60 min in an ice bath. 30 μL of the resulting catalyst ink was then cast on the

glassy carbon electrode, and the final catalyst loading on the electrode was 0.75 mg cm^{-2} . For the benchmark Pt/C (Alfa Aesar, 20 wt%), the Pt loading was controlled as 0.02 mg cm^{-2} . A saturated calomel electrode (SCE) was used as the reference electrode. A graphite rod was employed as the counter electrode. All the potentials used in this work were converted versus the reversible hydrogen electrode (RHE). The zero point of the RHE was calibrated by the equilibrium potential of HOR/HER of 20% Pt/C catalyst in H_2 -saturated electrolyte. iR correction is applied for all polarization curves, and the solution resistance was measured via electrochemical impedance (100 kHz to 100 Hz).

The poisoning experiments were conducted using chronoamperometry at 0.09 V. For the CO-stripping voltammetry, a monolayer of CO was firstly adsorbed onto the catalyst's surface by holding at 0.1 V for 10 min. The electrolyte was then flushed with Ar for 20 min to remove dissolved CO completely. Then, the adsorbed CO was stripped by scanning between 0.05 and 1.0 V at a scan rate of 50 mV s^{-1} .

2.5. Calculation of the kinetic current and the exchange current density

The $j_{k@50 \text{ mV}}$ was the kinetic current density of electrode at $\eta = 50 \text{ mV}$. The j_k is the geometric area normalized value of i_k . The i_k was calculated by the Koutecky-Levich equation,

$$\frac{1}{i} = \frac{1}{i_k} + \frac{1}{i_d}$$

Where i is the measured current at a potential, i_k is the calculated kinetic current, i_d is the diffusion current. The i_d can be calculated by the Nernstian diffusion equation.

$$\eta_d = -RT \left/ 2F \ln \left(1 - \frac{i_d}{i_l} \right) \right.$$

Where η_d is the over-potential of the electrode, R is the ideal gas constant ($8.314 \text{ J mol}^{-1} \text{ K}^{-1}$), T is the temperature (in Kelvin). F is the Faraday constant (96485 C mol^{-1}), i_l is the diffusion limiting current, which can be described by Levich equation.

$$i_l = 0.62nFAD^{2/3}\nu^{-1/6}c_0\omega^{1/2}$$

Where n is the number of transferred electrons of the reaction, A is the geometric area of the electrode, D is the H_2 diffusion constant in the electrolyte, c_0 is the concentration of H_2 , ω is the rotation speed of the electrode, and ν is the kinetic viscosity.

The $j_{0,\text{disk}}$ was defined as the exchange current density normalized to RDE geometric area. The exchange current density (j_0) was calculated by fitting the Butler-Volmer equation.

$$j_k = j_0 \left(e^{\frac{\alpha F \eta}{RT}} - e^{-\frac{\beta F \eta}{RT}} \right)$$

Where j_k is the kinetic current density of the electrode, η is the overpotential of the electrode. α and β is the transfer coefficient of anode and cathode, respectively. And $\alpha + \beta = 1$ was set in the calculation.

2.6. MEA tests

The membrane electrode assembly (MEA) was prepared by using an ink spray method. Ni@NC was employed as anode catalyst and commercial Pt/C (40%, Johnson Matthey) or Ag/C (40%, Premetek) as cathode catalyst. The catalyst ink was prepared by ultrasonically dispersing the catalysts and ionomer (PAP-TP-100, 3.5 wt% in ethanol, Versogen) into water and isopropanol (1:20 v/v) for 1 h. The I/C ratio of the catalyst ink was maintained at 0.7. Then the anode ink was sprayed onto the gas diffusion layer (GDL, TGP-H-060, Toray) with a hand spray brush to reach a loading of $ca. 5 \text{ mg}_{\text{Ni}} \text{ cm}^{-2}$ with an active area of 1 cm^2 . The cathode ink was sprayed onto cathodic sides of the PAP-TP-85 membrane (Versogen) with another hand spray brush to reach a loading of $0.4 \text{ mg}_{\text{Pt}} \text{ cm}^{-2}$ or $0.4 \text{ mg}_{\text{Ag}} \text{ cm}^{-2}$. Three airbrushes were used

to prevent the possible cross-contamination. The catalyst loading was measured by analytical balance and further verified by ICP-OES. The GDL for the cathode side was SGL-29 BC from SGL. The cathode catalyst coated membrane as well as the anode catalyst coated GDL was immersed in 2 M KOH for 12 h and then rinsed with deionized water. The MEA was assembled without hot-pressing. Single serpentine graphite bipolar plates were used to hold the MEA. $180 \mu\text{m}$ of nylon-reinforced PTFE gasket was placed on each side of the MEA to ensure tight closure. The applied torque was fixed at 5.0 Nm using a torque wrench. The compression ratio of GDL was estimated at 20–25%. The fuel cell performance was tested on a fuel cell test station (850e, Scribner) equipped with a backpressure module. The anode, cathode humidifier temperatures, and the cell temperature were 78, 80, and 80°C , respectively. The anode relative humidity was 92%, and the cathode relative humidity was 100%. The back pressure was set as 2.0 bar, and the flow rates of H_2 and O_2 were both 300 sccm.

3. Results and discussion

3.1. Catalyst synthesis and characterization

To understand the role of the carbon shell on the Ni nanoparticles, three Ni-based catalysts, Ni@NC, C encapsulated Ni nanoparticles (Ni@C) and Ni nanoparticles without carbon layers (i.e., Ni nanoparticles supported on carbon, denoted as Ni/C), were synthesized.

A facile sol-gel method was developed to synthesize the Ni@NC catalyst. Nickel nitrate and Ketjen ECP600 carbon were selected as the metal precursor and carbon support, respectively. Citric acid was selected as the reducing agent, competitive adsorbent, and more importantly, the source of carbon coating. Urea was introduced as N source to dope the carbon shell. The final Ni@NC catalysts were obtained by pyrolysis in N_2 atmosphere. We have optimized the pyrolysis temperature for the formation of the NC shells on Ni nanoparticles. At a lower temperature, such as $300\text{--}400^\circ\text{C}$, only NiO nanoparticles can be obtained (TEM image and XRD pattern are shown in Fig. S1). In contrast, at the too high reaction temperature, i.e., $800\text{--}1000^\circ\text{C}$, the carbon shell would break, and the metal tends to leak out and aggregate to form large particles (TEM image and XRD pattern are shown in Fig. S2). The optimized temperature was found as 550°C . At this temperature, well-defined Ni nanoparticles encapsulated in NC shells were obtained.

Fig. 1a shows the transmission electron microscopy (TEM) image of the as-obtained Ni@NC catalysts. It shows the uniform nanoparticles with the diameter of *ca.* 6 nm well dispersed on carbon supports. Fig. 1b shows the high-resolution transmission electron microscopy (HRTEM) image. Crystalline nanoparticles were clearly observed. The lattice fringes with an interplanar spacing of 0.21 and 0.18 nm were assigned to the (111) and (200) facets of Ni, respectively. Carbon shells, which are composed with 1–4 graphene layers (see the statistical analysis in Fig. S3), were clearly observed on the surface of the Ni nanoparticles. The lattice fringes of the shell with an interplanar spacing of 0.34 nm were attributed to the (002) facet of graphite. High-angle annular dark-field scanning TEM (HAADF-STEM) elemental mapping was used to investigate the composition of Ni@NC and the elemental distributions (Fig. 1c). It was found that C, N, and O overlapped Ni's mapping area and it roughly followed the profile of Ni@NC particles. The N-doping to carbon was further confirmed by the XPS results (Fig. S4a), in which a peak assigned to N 1 s was clearly observed at 400.2 eV, and the N amount was calculated as 1.1 at% (Table S2). A peak assigned to C–N was also found in the C 1 s XPS spectra (Fig. S4b). Fig. 2a shows the XRD pattern of the as-obtained Ni@NC catalysts. It shows that metallic Ni was successfully obtained. The Ni content in Ni@NC was determined as 55 wt% by TGA analysis (Fig. S5).

The Ni@C was synthesized by using a similar procedure without adding N source. The XRD pattern (Fig. 2a) shows that metallic Ni was obtained, and the TEM images (Fig. S6) demonstrated the obtained well-dispersed nanoparticles with clear carbon shells encapsulated on them.

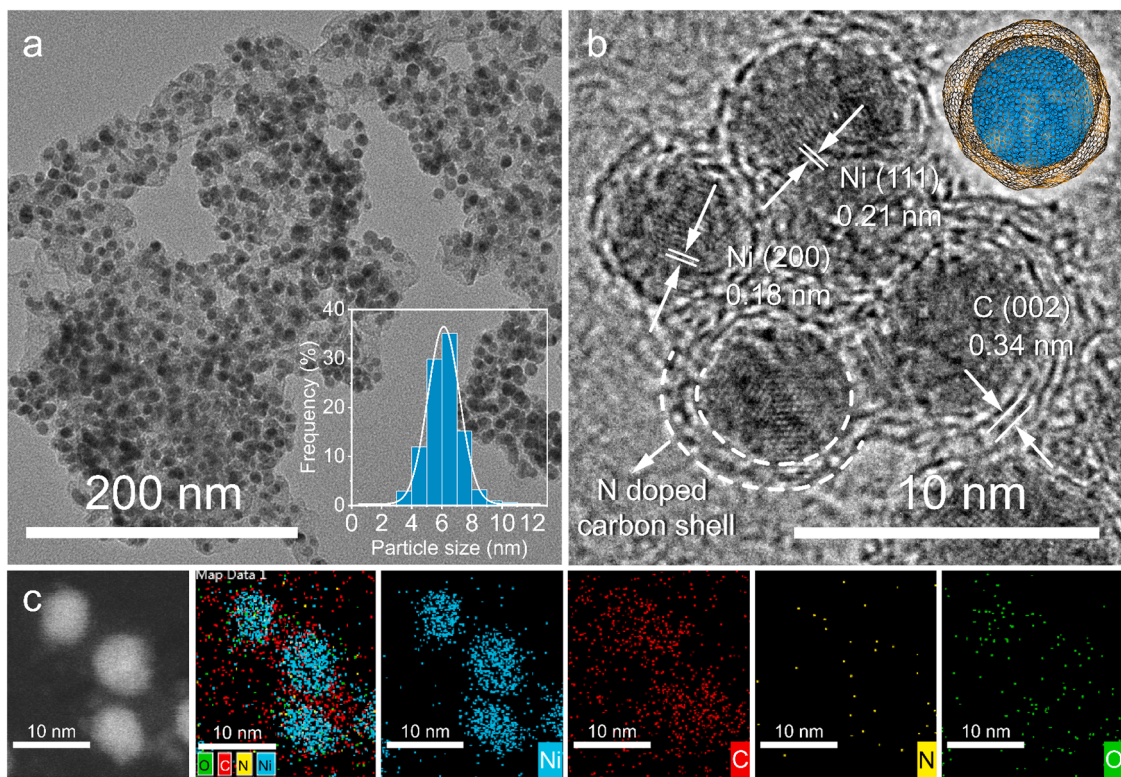


Fig. 1. Electron microscopy characterizations of the Ni@NC. (a) TEM image. Insert is a statistical histogram of the size of the particles. (b) HRTEM image. Inset is the schematic illustration of the structure of Ni@NC. (c) HAADF-STEM elemental mapping image.

Compared with Ni@NC, Ni@C has fewer defects due to the lack of N doping. The defects were characterized by Raman spectra (Fig. 2b). The peaks at around 1344 cm^{-1} , designated as the D-band, are associated with the disordered carbon structure; the peaks at approximately 1589 cm^{-1} , assigned to the G-band, are related to the in-plane vibration of sp^2 bonded carbon [49]. The $I_{\text{D}}/I_{\text{G}}$ value is 1.01 and 0.93 for Ni@NC and Ni@C, respectively, confirming Ni@NC possessed more defects than Ni@C. The Ni/C was synthesized by hydrothermal method. The XRD pattern (Fig. 2a) illustrated the formation of the metallic Ni and the TEM images (Fig. S7) exhibited the Ni nanoparticle with the size of ca. 12 nm dispersed on carbon supports.

For the three samples of Ni@NC, Ni@C and Ni/C, although similar XRD patterns show that metallic Ni was obtained (Fig. 2a), the surface environments are different. Fig. 2c shows the high-resolution Ni 2p XPS spectrum of the three samples. For Ni@NC and Ni@C, the main peak respectively located at 852.7 and 852.2 eV, which were assigned to Ni⁰ species [42]. The slightly higher binding energy for the Ni in Ni@NC may be attributed to the high electronegativity of the doped N, which attracted electrons from Ni [50,51]. However, for the Ni/C, the main peaks that appeared at 856.2 and 862.1 eV were assigned to Ni²⁺ and satellites. It demonstrated that the Ni is easy to be oxidized without carbon shell protection.

To further understand the influence of the carbon shells to the core Ni nanoparticles, the X-ray absorption spectroscopy (XAFS) was conducted. Fig. 2d presents the X-ray absorption near-edge structure (XANES) of Ni@NC and Ni@C, as well as the Ni foil and NiO as references. The absorption edges of Ni@NC and Ni@C were close to that of Ni foil, suggesting the nearly metallic form of Ni, beneficial from the protection of the carbon shells. Because of the different electronegativity of C and N to Ni, slightly positive shifts of the absorption edges of Ni@NC and Ni@C were observed. A larger shift was observed for Ni@NC, demonstrating the higher interaction between Ni and NC, which is consistent with the XPS results. The radial structure function around Ni was determined by k^3 -weighted Fourier transform (FT) of extended X-

ray absorption fine-structure (EXAFS) spectra (Fig. 2e and Fig. S8). The peaks located at ~ 2.2 and 1.7 \AA were ascribed to the Ni-Ni and Ni-O bond, respectively, as indicated by the Ni foil and NiO references [46]. The absence of peaks in $\sim 1.7\text{ \AA}$ suggests the Ni@NC and Ni@C samples without the existence of Ni-O bond [46]. The decrease in peak intensity as compared to Ni-Ni bonds in Ni foil indicates the damped coordination structure of Ni [43]. The fitting result (Fig. S9 and Table S3) of Ni K-edge EXAFS shows the first-shell Ni-Ni coordination numbers (CNs) decreased from Ni-foil (~ 12) to Ni@C (~ 9.2) and Ni@NC (~ 8.4). The decrease of the CNs in Ni@C and Ni@NC was attributed to the lower crystallinity of the nanoparticles and the coordination of Ni to the encapsulated carbon layers. Corresponded to the major peak in R space, the EXAFS wavelet transform (Fig. 2f) shows only one intensity maximum at $\sim 8.0\text{ \AA}^{-1}$ in k space, further confirming the metallic nature of Ni in Ni@NC and Ni@C.

3.2. High HOR performance of the Ni@NC and stable HEMFC performance achieved by using Ni@NC as the anode catalyst

The HOR performances of Ni@NC and control samples were evaluated using a rotating disk electrode system in H_2 -saturated 0.1 M KOH electrolyte. Fig. 3a shows the polarization curves of the Ni@NC, the control samples, and commercial Pt/C benchmark. An anodic current was observed when positive overpotential was applied. Compared with the polarization curve obtained in Ar-saturated electrolyte (Fig. S10a), the anodic current was attributed to the hydrogen oxidations. Ni@NC shows the highest HOR current in the three Ni-based catalysts. Ni/C shows a slightly lower HOR current, and Ni@C shows a much lower HOR current compared with Ni@NC. We calculated the kinetic current density at 50 mV (vs. RHE, the same hereafter), and they are denoted as $j_{\text{k}}@50\text{ mV}$ and summarized in Fig. S11. The Ni@NC shows the highest $j_{\text{k}}@50\text{ mV}$ of $1.92\text{ mA cm}_{\text{disk}}^{-2}$, which is 1.6 and 10.6 times of Ni/C and Ni@C, respectively. To understand the intrinsic activity of the three Ni-based catalysts, we calculated the electrochemical surface area (ECSA)

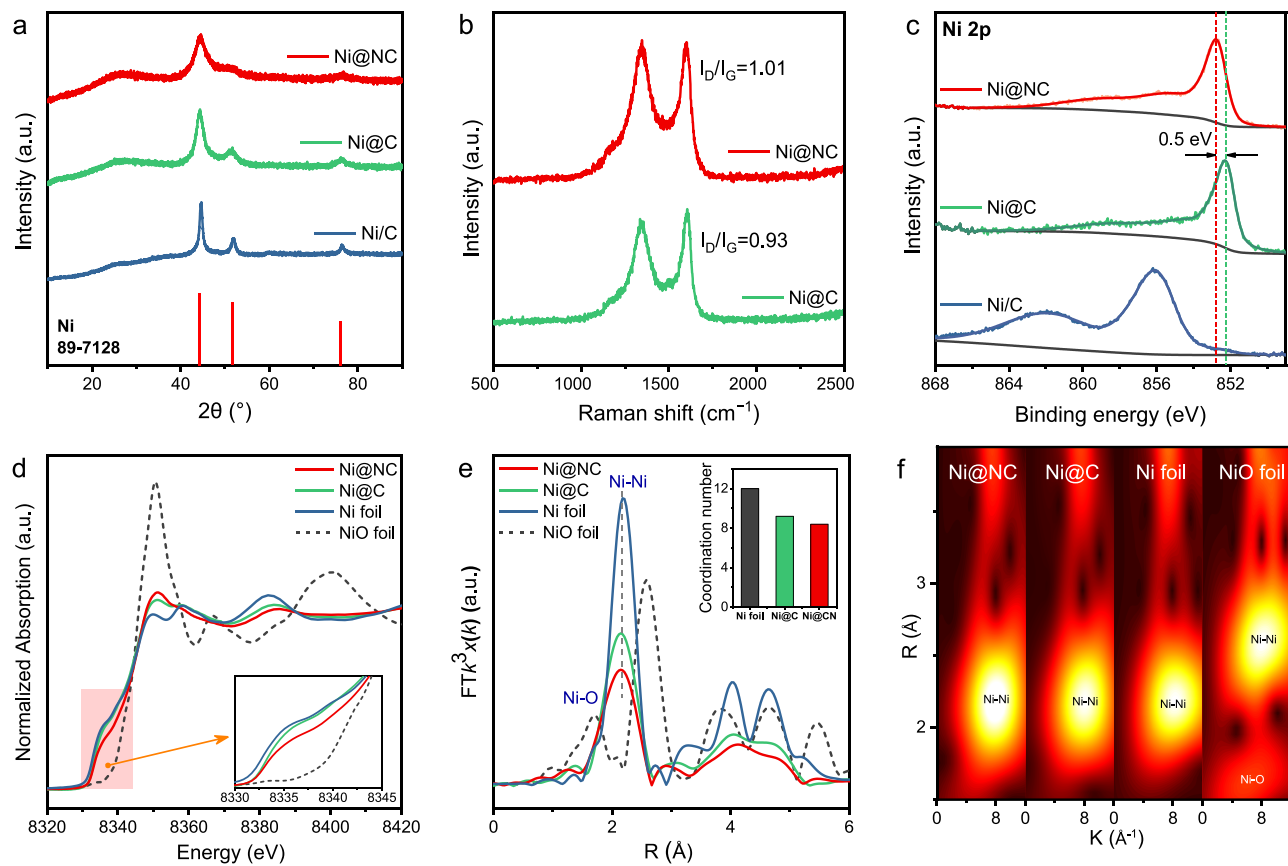


Fig. 2. (a) XRD patterns of Ni@NC, Ni@C, and Ni/C. (b) Raman spectroscopy curves of Ni@NC and Ni@C. (c) High-resolution Ni 2p XPS spectra of Ni@NC, Ni@C, and Ni/C. (d) Ni K-edge XANES spectra and (e) corresponding Fourier transforms of k^3 -weighted EXAFS spectra for Ni@NC, Ni@C, Ni foil and NiO foil. Insert in (e) is the coordination numbers in the first coordination shell of Ni atoms for Ni foil, Ni@C and Ni@NC by EXAFS spectra curve fitting. (f) Wavelet transforms of k^3 -weighted EXAFS spectra of Ni K-edge.

normalized exchange current density (j_0). The ESCAs were calculated by the charge transferred from the reduction of $\text{Ni}(\text{OH})_2$ to Ni divided by the constant of $514 \mu\text{C cm}^{-2}$ [52] (Fig. S12). The ECSA of Ni@NC and Ni/C are measured at the similar level of $5.4 \text{ cm}^2 \text{ Ni}$ and $3.5 \text{ cm}^2 \text{ Ni}$, respectively. However, the Ni@C showed a much lower ECSA of $0.85 \text{ cm}^2 \text{ Ni}$, due to the block effect of the carbon shell. The calculated ECSA normalized j_0 were summarized in Fig. S11, and all of the three Ni-based catalysts showed similar j_0 of ca. $35 \mu\text{A} \cdot \text{cm}_{\text{Ni}}^{-2}$. It revealed the metal Ni principally constitutes active sites for all three Ni-based catalysts.

One of the most significant drawbacks of Ni-based catalysts is their low durability. Ni tends to be oxidized in the alkaline electrolyte under high potential, and thus losing its HOR activity. And it became worse when the materials with large specific surface areas (e.g., Raney nickel and nickel nanoparticles) [53,54]. The Ni@NC shows significantly improved stability. A chronoamperometry test at 0.09 V was conducted to investigate the stability of the Ni-based catalysts (relative current curve shown in Fig. 3b and the absolute current values shown in Fig. S13). The current density for Ni@NC shows almost no change, but it decayed about 15% for Ni/C. We also evaluated the stability by using the accelerating durability test (ADT), which cycled the catalysts between $\sim 10 \text{ mV}$ and 100 mV . The relative $j_{\text{K}}@50 \text{ mV}$ only decreased by 35% for the Ni@NC after 30,000 cycles, while it decreased by 84% after only 20,000 cycles for Ni/C (Fig. 3c).

HEMFC membrane electrode assemblies (MEAs) were assembled by using respective Ni@NC, Ni/C, and Ni@C as anode catalysts, and their performances are shown in Fig. 3d. Ni@NC catalyst exhibits good HEMFC performance with an open circuit voltage up to 1.06 V , maximum current density of 150 mA cm^{-2} , and peak power density of

66 mW cm^{-2} . Due to the low HOR activity of Ni@C, only a low peak power density of 12 mW cm^{-2} could be reached. By using Ni/C, the HEMFC has a similar performance at the low current density region to the Ni@NC HEMFC. However, the cell voltage dropped seriously when the current density was higher than 50 mA cm^{-2} , which was caused by the passivation of the Ni/C anode catalyst. A workable PGM-free HEMFC was fabricated by using Ni@NC as anode and Ag/C as cathode (Fig. S14). A long-term fuel cell durability test was conducted at 0.7 V (Fig. 3e). By using Ni@NC, it can stably operate for more than 200 h. The current density degradation rate is only $0.04 \text{ mA cm}^{-2} \text{ h}^{-1}$, illustrating the high stability of the Ni@NC catalyst. In comparison, the Ni/C HEMFC shows much worse durability, which failed (lost 90% of the initial cell current) after only 7 h of operation. The high frequency resistance (HFR) analysis illustrated the Ni@NC HEMFC maintained a relatively lower HFR value during the whole test, while the HFR for the Ni/C HEMFC increased dramatically and became very noisy after about 7 h of operation (Fig. S15), because of the low current. It demonstrated that the Ni@NC has much enhanced stability under the fuel cell working condition, which is beneficial from the protection of the NC shells. Table S4 summarized the performance of the reported HEMFC using Ni-based anode, and the Ni@NC showed competitive stability. We characterized the Ni@NC catalysts after durability test, and it was found that the NC shells were retained (Fig. S16a and b). The C 1 s XPS spectra show slight oxidation of the carbon shell (Fig. S16c and Table S5). The crystalline phase and valence state of the tested Ni@NC almost unchanged after the stability tests, indicating by the XRD pattern and XPS spectra shown in Fig. S16d and e, respectively.

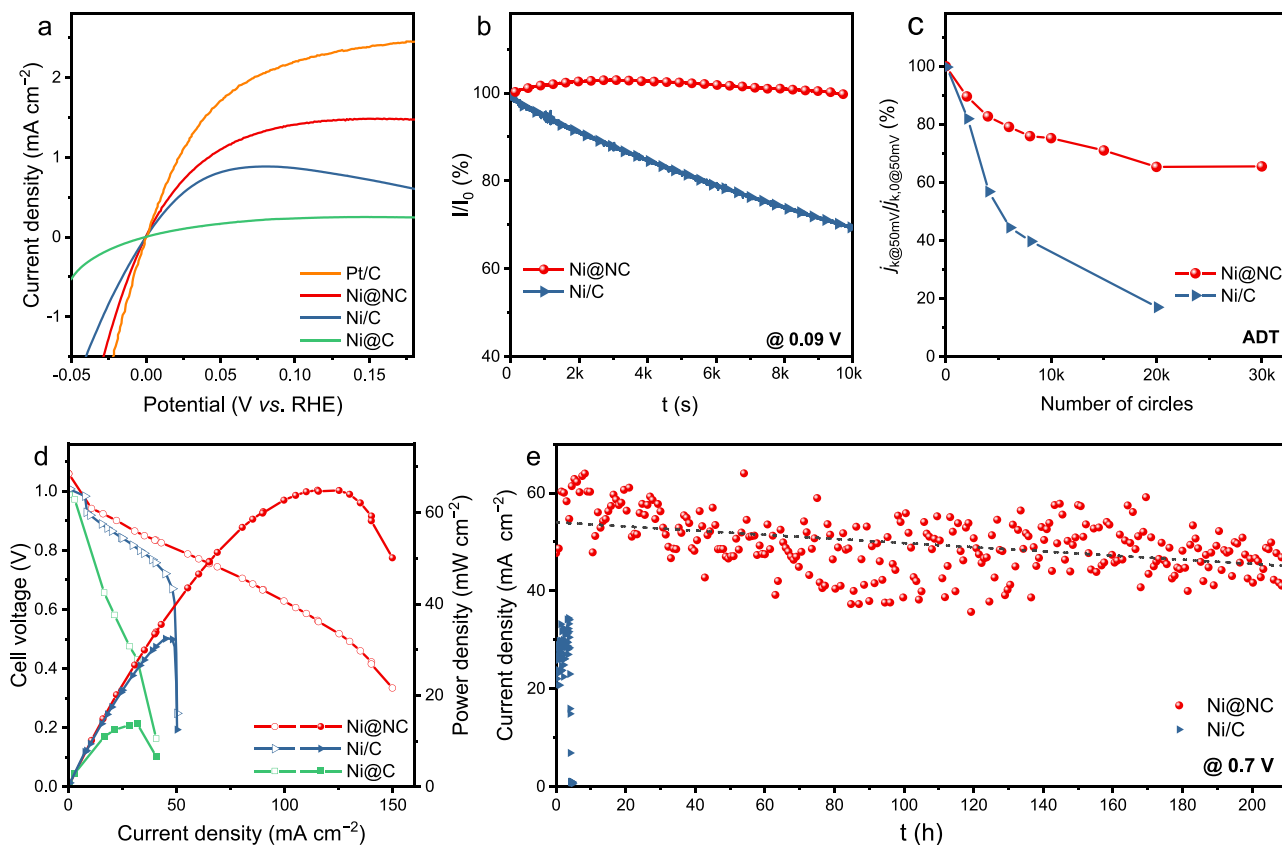


Fig. 3. HOR activity tested by the RDE method and the HEMFC performance by using the Ni-based catalysts as anode. (a) Polarization curves of Ni@NC, Ni@C, Ni/C and commercial Pt/C in H₂-saturated 0.1 M KOH. The rotating speed was 1600 rpm and the scan rate was 1 mV s⁻¹. (b) Chronoamperometry test of Ni@NC and Ni/C in H₂-saturated 0.1 M KOH at 0.09 V. The current was normalized to its initial value; (c) The relative $j_{k@50\text{ mV}}/j_{k@50\text{ mV}}$ of Ni@NC and Ni/C after accelerating durability test, which cyclic between -10–100 mV with a scan rate of 100 mV s⁻¹. (d) H₂/O₂ HEMFC polarization and power density curves with Ni@NC, Ni/C, or Ni@C anode. The anode catalyst loading was 5 mg_{Ni} cm⁻², and the cathode catalyst loading was 0.4 mg_{Pt} cm⁻² using commercial 40% Pt/C. The anode, cathode humidifier temperatures, and the cell temperature were 78, 80, and 80 °C, respectively. The back pressure was 2.0 bar, and the flow rate of H₂ and O₂ was both 300 sccm. (e) Fuel cell stability test at 0.7 V with Ni@NC or Ni/C anode. The anode, cathode humidifier temperatures, and the cell temperature were 78, 80, and 80 °C, respectively. The back pressure was 2.0 bar, and the flow rate of H₂ and O₂ was both 300 sccm.

3.3. High tolerance to the poisoner in H₂ of the Ni@NC

More importantly, the Ni@NC showed enhanced anti-poisoning ability, which may allow the HEMFC to be fed by low-cost crude H₂. CO is the major poisoner in crude H₂ for fuel cells, which significantly reduces the performance on the anode. The chronoamperometry tests were first employed to investigate the anti-poisoning ability in 0.1 M KOH electrolyte. As shown in Fig. 4a and Fig. S17a, after the introduction of 100 ppm of CO, the current density gradually reduced by using Ni/C or Pt/C catalysts, demonstrating the poisoning effects. In contrast, the current density was maintained well by using Ni@NC, and it still remained 92% in exposure to CO for 2600 s, illustrating the good ability for anti-CO poisoning. We also tested HOR performance with different CO concentrations, and the chronoamperometry curve is shown in Fig. 4b and Fig. S17b. With a high concentration of 3200 ppm of CO at the end of the test, the HOR current density catalyzed by Ni@NC retained as 75% for a 1400 s test. In the same condition, the current density was only less than 25% by using Ni/C or Pt/C. We also tested the HOR polarization curves in H₂-saturated electrolytes by using the catalyst after the CO durability test (Fig. S18). After the test with 100 ppm of CO, the polarization curve of Ni@NC almost resembles the curve tested before the poisoning test, demonstrating a good tolerance to CO. In comparison, the Ni/C and Pt/C showed much depressed HOR activity, illustrating the irreversible poisoning effect of CO. After exposure to a high concentration of CO (3200 ppm), Ni/C and Pt/C lost nearly all their HOR activity, showing a sharp decrease in current

density of 92% and 93%. In contrast, the Ni@NC only dropped 37%, indicating a robust performance under extreme poisoning atmosphere.

Besides CO, the Ni@NC also showed good anti-poisoning ability to S²⁻ and SCN⁻, which are common impurities in crude H₂. As shown in Fig. 4c and Fig. S17c, the S²⁻ heavily poison the Pt/C catalysts; however, it has almost no influence on Ni@NC. With SCN⁻, the performance of Pt/C and Ni/C dropped more than 60%, while it only dropped less than 20% for Ni@NC (Fig. 4d and Fig. S17d). The HOR performance of Ni@NC could be recovered by switching the electrolyte back to 0.1 M KOH, but the Ni/C and Pt/C could not be recovered, indicating a permanent poisoning (Fig. S19).

3.4. High HEMFC performance by using Ni@NC as anode catalyst and feeding H₂ with CO

Encouraged by the good anti-poisoning ability of the Ni@NC, we tested the HEMFC by feeding H₂ with 100 ppm of CO (500 times to the limitation in the current standard for fuel cell used H₂, Table S1) at the anode. In Fig. 5a, the polarization and power density curves show Ni@NC maintains most cell performance under H₂/CO purge, whose open circuit voltage maintained at 1.06 V and the current density persisted reached 78 mA cm⁻² @ 0.7 V (95% percentage as before). Fig. 5b shows the performance of HEMFC with different anode catalysts by feeding H₂ with 100 ppm of CO. The Ni@NC cell delivered a peak power density to 58 mW cm⁻² by feeding H₂ with 100 ppm of CO, which has surpassed the cell performance by using Ni/C (9 mW cm⁻²) or Pt/C

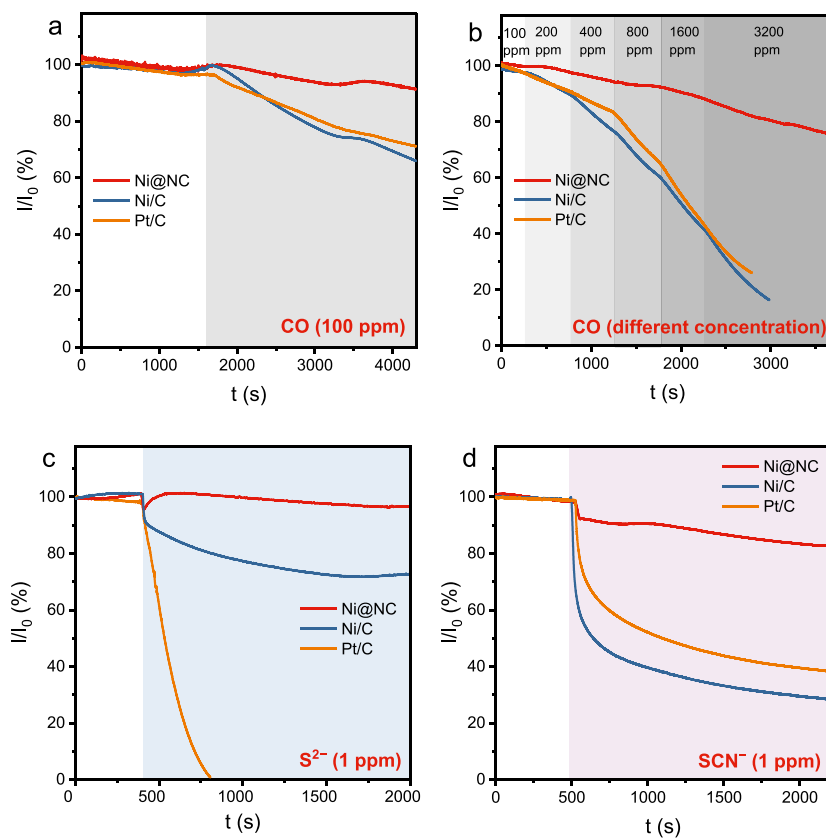


Fig. 4. The anti-poisoning HOR performances. Chronoamperometry curves at 0.09 V in H₂-saturated 0.1 M KOH of Ni@NC, Ni/C and Pt/C before and after the addition (shaded area) of (a) 100 ppm CO, (b) different concentrations of CO, (c) 1 ppm K₂S, and (d) 1 ppm KSCN. The current densities were normalized to their initial values.

(25 mW cm⁻²). The HFR analysis shows Ni@NC almost unchanged when purged with H₂ or H₂/CO (Fig. S20a and b). It demonstrated the advantages of Ni@NC catalysts when feeding the crude H₂. Although the Pt/C catalysts have high HOR performance and the Pt/C HEMFC showed high power density when feeding ultrapure H₂ (Fig. S21), the CO heavily poisoned the Pt/C catalysts and it showed worse HEMFC performance than Ni@NC when feeding gas with CO. To evaluate the antitoxic stability, a 24 h operation was carried out under H₂/CO feeding gas at 0.7 V, and the relative current densities were shown in Fig. 5c. It was found only ca. 7% cell performance decreased after CO introduction, and then it became stable for the rest of the time for the Ni@NC cell. In contrast, Ni/C and Pt/C experienced a sharp decrease by ca. 75% after CO purged, displaying the severe poisoning by CO. After the 24 h of CO poisoning test, we switched back the anode feeding gas to pure H₂. Only Ni@NC cell can fully recover the initial cell performance, while both Ni/C and Pt/C merely showed a slight recovery. The results demonstrated the advantage of Ni@NC in the fuel cell working condition using crude H₂.

3.5. The mechanism for the high performance of the Ni@NC

The high activity, stability and anti-poisoning ability of Ni@NC were attributed to the unique NC shells, which protected the HOR active Ni nanoparticles. The anterior results show that bare Ni/C has high HOR activity, but it is not stable and easy to be poisoned. The Ni nanoparticles in Ni@C are well protected by the highly graphitized carbon shell, but the carbon shell blocked the reactant for the HOR process as well, leading to low activity. This is proved by the ultralow ECSA of the Ni@C (Fig. S12). For the Ni@NC, it has the optimal NC shell, which has high permeation of H₂ and proton and thus guarantees the HOR process, but blocks the oxidation agent and poisoners, making the Ni@NC have high

stability and anti-poisoning ability. A scheme illustrating the characterization of the three Ni-based catalysts is shown in Fig. 6a.

N doping could lower the graphitization degree and create more defects [55,56]. The previous studies have shown that wrinkles and other defects can accelerate the permeation of H₂ [57,58] and lowering barriers for H⁺ transport [59,60] on graphene, which is feasible for the HOR/HER process. The permeability of H⁺ was investigated by acid washing experiment. If the H⁺ can easily go through the shell, the Ni nanoparticles would be dissolved. By leaching Ni@NC and Ni@C in 0.1 M HCl for 12 h at room temperature, we found most of the inner Ni in Ni@NC were leached out but all Ni cores in Ni@C kept complete and unattakable (Fig. S22), which demonstrated the enhanced H⁺ permeability for the NC shell.

The H₂ (2.89 Å) [61] and H⁺ (0.28 Å) [62] have very small sizes, compared with other species, such as O₂ (3.46 Å) [61], CO (3.76 Å) [61], hydrated S²⁻ (3.24 Å) [63] and SCN⁻ (3.35 Å) [64]. Graphene with selective H₂ permeability with O₂ [65], N₂ [65], CH₄ [66], CO [66], or CO₂ [67] were reported. This selectivity was relevant to their different molecule kinetic diameters [65,68], where the transport activation barriers increase quadratically with molecules' kinetic diameter [58]. Thus, by carefully adjusting the pores of graphene, selective permeation of H₂/H⁺ could be achieved [66].

The enhanced stability of Ni@NC was attributed to the block of the O₂, which could oxidize the Ni nanoparticles and thus deactivate the catalysts. This process can also be considered as the catalyst poisoned by oxygen. We evaluated the anti-oxidation ability by immersing electrodes in an O₂-saturated water, and then tested their HOR activity. As shown in Fig. S23a and b, a significant degradation was observed for Ni/C after only 0.5 h of treatment, while the Ni@NC only had slight degradation after 24 h of treatment. The $j_{0,disk}$ of the catalysts with different O₂ treatment times were summarized in Fig. S23c. The Ni@NC showed a

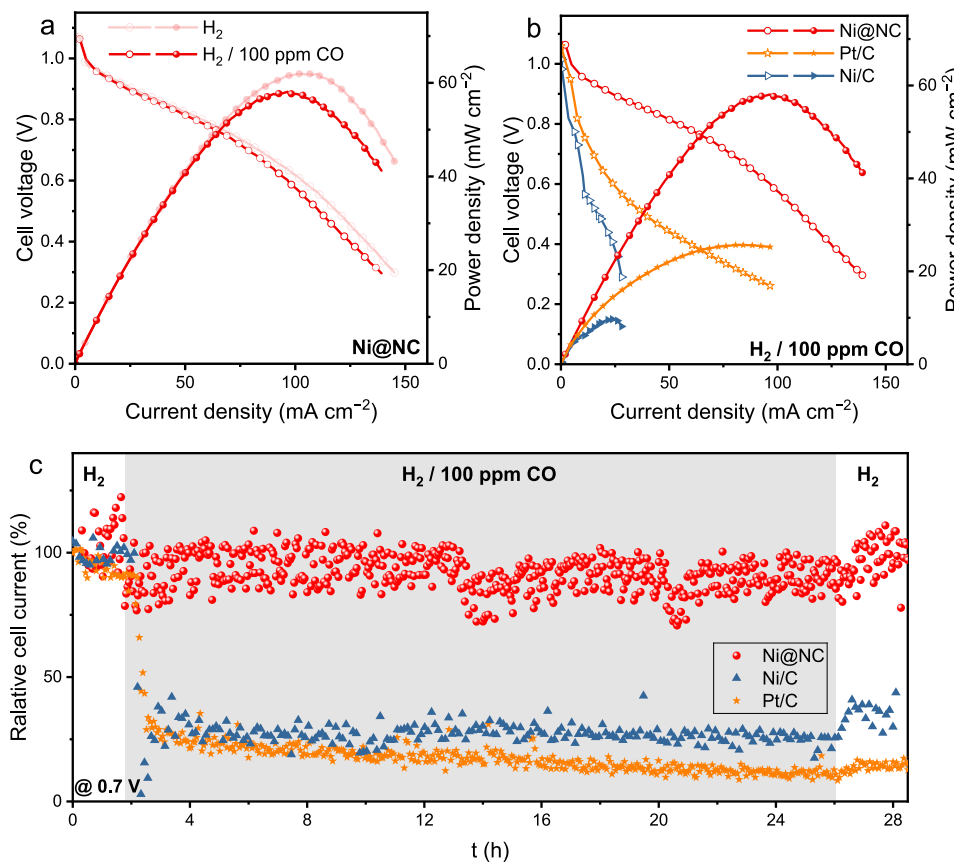


Fig. 5. HEMFC performance by feeding H₂ with CO. (a) HEMFC polarization and power density curves using Ni@NC anode feeding by H₂ with and without 100 ppm of CO. (b) HEMFC polarization and power density curves using Ni@NC, Ni/C and Pt/C anode feeding by H₂ with 100 ppm of CO. (c) The HEMFC chronoamperometric curve at 0.7 V. In the shade region, the anode feeding gas was switch to H₂ with 100 ppm of CO. For all the tests, the anode catalyst loading was 5 mg_{Ni} cm⁻² for both Ni@NC and Ni/C, and 0.2 mg_{Pt} cm⁻² for Pt/C. The cathode catalyst loading was 0.4 mg_{Pt} cm⁻² of Pt/C. The anode, cathode humidifier temperatures, and the cell temperature were 78, 80, and 80 °C, respectively. The back pressure was 2.0 bar, and the flow rate of H₂/100 ppm CO and O₂ were both 300 sccm.

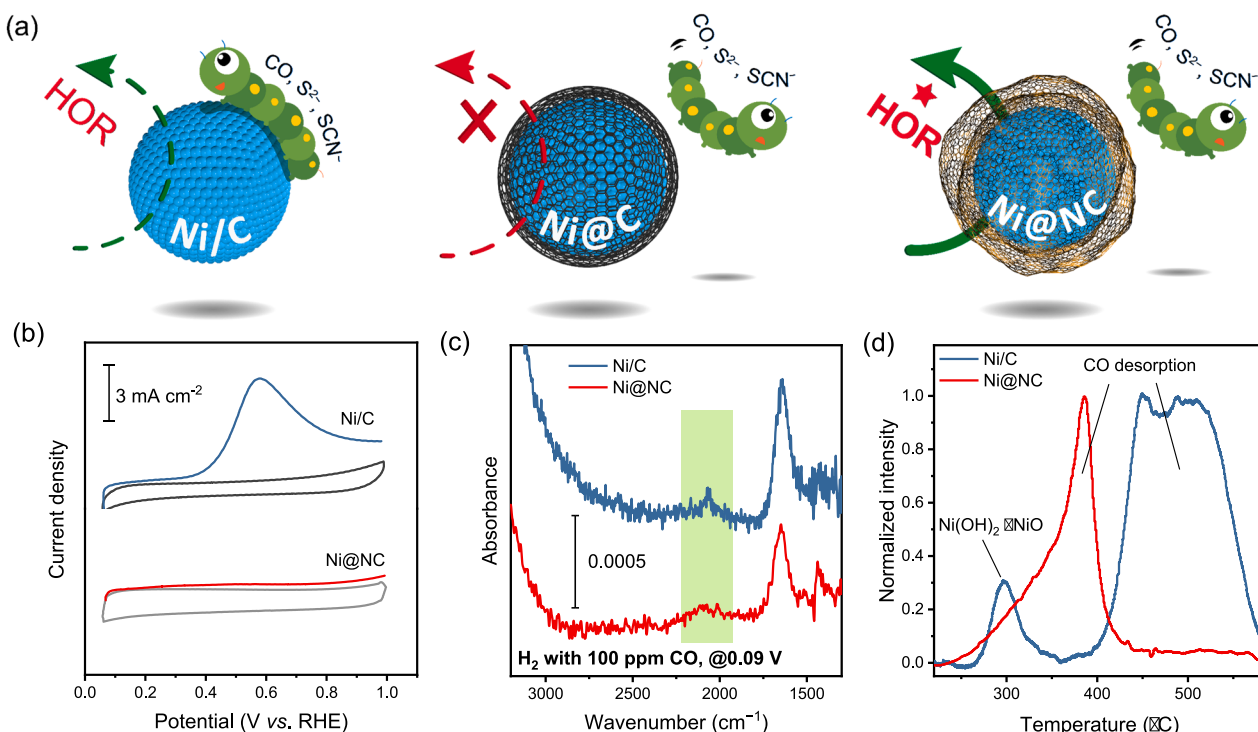


Fig. 6. The anti-poisoning analyses. (a) Scheme to show the characteristics of the three Ni-based HOR catalysts. (b) CO-stripping curves of Ni@NC and Ni/C. (c) The electrochemical *in situ* ATR-SEIRAS spectra of Ni/C and Ni@NC in H₂ with 100 ppm of CO saturated 0.1 M KOH electrolyte. (d) CO-TPD curves of Ni@NC and Ni/C.

very low degradation rate of 1.1×10^{-4} mA cm $^{-2}$ min $^{-1}$, which was about two orders of magnitude slower than that of Ni/C, demonstrating the enhanced anti-oxidation property of Ni@NC.

The anti-poisoning ability was attributed to the weakened adsorption of the CO and other species on the surface of the catalysts, which is caused by the hindrance of the NC shells. The CO adsorption was firstly examined by the CO-stripping experiment (Fig. 6b). A large CO stripping peak was observed for the Ni/C, demonstrating a significant amount of CO adsorbed on the surface of Ni/C. In comparison, the Ni@NC shows almost no CO oxidation current, demonstrating almost no CO adsorbed by Ni@NC. To further confirm the weak adsorption of CO on the Ni@NC during the HOR process, electrochemical *in situ* attenuated total reflection surface enhanced infrared reflection absorption spectroscopy (ATR-SEIRAS) has been employed. The Ni@NC or Ni/C catalyst was deposited to the Au surface on the ATR crystal, and it was used as working electrode operated under 0.09 V in the H₂-saturated electrolyte with 100 ppm of CO. Fig. 6c shows the spectra. A peak at 2080 cm $^{-1}$ appeared for the Ni/C, which was assigned to the C-O vibration from linear adsorbed CO on the Ni surface [69–71]. It demonstrated the CO poisoned surface. However, the peak for Ni@NC was negligible, demonstrating seldom CO was adsorbed on the Ni surface. It revealed that NC shells depressed the adsorption of CO. We further conducted CO temperature programmed desorption (TPD), which probes the bonding between CO and catalyst [72]. As shown in the Fig. 6d, two peaks were observed for Ni/C. The peak at 300 °C was assigned to the dehydration process of oxidized Ni(OH)₂ to NiO. The peaks above 450 °C were assigned to the desorption of CO. For Ni@NC, it shows a CO desorption peak at 385 °C, which is lower than that for Ni/C, demonstrating easier desorption of CO on Ni@NC. All the experimental results indicated the weakened CO adsorption on the Ni@NC, leading to the high tolerance of CO.

4. Conclusion

In summary, a selectively permeable carbon layer protection strategy was demonstrated to enhance the anti-poisoning ability of the Ni-based HOR catalysts. An encapsulated catalyst, Ni@NC, was successfully synthesized and showed high stability and anti-poisoning ability for HOR in both RDE and HEMFC tests. By feeding H₂ with 100 ppm of CO, only the Ni@NC HEMFC showed consistent performance to that fed by high purity H₂, while the Ni/C or Pt/C HEMFCs showed significantly depressed performance. With the NC shell, selective permeance of H₂ but block of CO and other poisoners was achieved. The NC shell on the Ni@NC catalysts blocked the poisoners, making it had high tolerance to the poisoners. The binding of CO is much weakened on the Ni@NC, and thus its HOR performance showed slight impact in the presence of CO. The N doping introduced defects, and made the NC shell permeable for H₂, thus guaranteed the HOR process. These results showed that the encapsulated strategy is promising to fabricate highly robust catalysts, which was desired for practical applications.

CRediT authorship contribution statement

Xingdong Wang: Methodology, Investigation, Writing – original draft. **Jinjie Fang:** Investigation, Formal analysis, Conceptualization. **Xuerui Liu:** Methodology, Investigation. **Dong Wei:** Physicochemical characterization. **Yiquan Yin:** Physical characterization. **Hailong Wei:** Physical characterization. **Jinlin Zhang:** Methodology, Investigation. **Yufeng Zhang:** Physicochemical characterization. **Xuejiang Zhang:** Physicochemical characterization. **Wei Zhu:** Conceptualization, Formal analysis. **Zhongbin Zhuang:** Conceptualization, Methodology, Supervision, Writing – review & editing, Resources.

Declaration of Competing Interest

The authors declare that they have no known competing financial

interests or personal relationships that could have appeared to influence the work reported in this paper.

Data Availability

Data will be made available on request.

Acknowledgements

This work was financially supported by the National Key Research and Development Program of China (2019YFA0210300), the National Natural Science Foundation of China (21971008, 22101016), Beijing Natural Science Foundation (Z210016), and Fundamental Research Funds for the Central Universities (buctrc201916, buctrc201823).

Appendix A. Supporting information

Supplementary data associated with this article can be found in the online version at doi:10.1016/j.apcatb.2023.122442.

References

- [1] Z.W. Seh, J. Kibsgaard, C.F. Dickens, I. Chorkendorff, J.K. Norskov, T.F. Jaramillo, Combining theory and experiment in electrocatalysis: Insights into materials design, *Science* 355 (2017) eaad4998.
- [2] J.O.M. Bockris, The origin of ideas on a hydrogen economy and its solution to the decay of the environment, *Int. J. Hydrol. Energy* 27 (2002) 731–740.
- [3] S. Wang, S.P. Jiang, Prospects of fuel cell technologies, *Natl. Sci. Rev.* 4 (2017) 163–166.
- [4] A. Hassan, V.A. Paganin, E.A. Ticianelli, Pt modified tungsten carbide as anode electrocatalyst for hydrogen oxidation in proton exchange membrane fuel cell: CO tolerance and stability, *Appl. Catal., B* 165 (2015) 611–619.
- [5] G. Avgoustopoulos, T. Ioannides, CO tolerance of Pt and Rh catalysts: Effect of CO in the gas-phase oxidation of H₂ over Pt and Rh supported catalysts, *Appl. Catal., B* 56 (2005) 77–86.
- [6] X. Wang, Y. Li, Y. Wang, H. Zhang, Z. Jin, X. Yang, Z. Shi, L. Liang, Z. Wu, Z. Jiang, W. Zhang, C. Liu, W. Xing, J. Ge, Proton exchange membrane fuel cells powered with both CO and H₂, *Proc. Natl. Acad. Sci. USA* 118 (2021), e2107332118.
- [7] B.M. Besancon, V. Hasanov, R. Imbault-Lastapis, R. Benesch, M. Barrio, M. J. Mølnvik, Hydrogen quality from decarbonized fossil fuels to fuel cells, *Int. J. Hydrol. Energy* 34 (2009) 2350–2360.
- [8] K. Narusawa, M. Hayashida, Y. Kamiya, H. Roppongi, D. Kurashima, K. Wakabayashi, Deterioration in fuel cell performance resulting from hydrogen fuel containing impurities: poisoning effects by CO, CH₄, HCHO and HCOOH, *JSAE Rev.* 24 (2003) 41–46.
- [9] R. Mohtadi, Wk Lee, S. Cowan, J.W. Van Zee, M. Murthy, Effects of hydrogen sulfide on the performance of a PEMFC, *Electrochim. Solid-State Lett.* 6 (2003) A272.
- [10] Z. Shi, D. Song, J. Zhang, Z.-S. Liu, S. Knights, R. Vohra, N. Jia, D. Harvey, Transient analysis of hydrogen sulfide contamination on the performance of a PEM fuel cell, *J. Electrochim. Soc.* 154 (2007) B609.
- [11] T. Wang, Z.-X. Chen, S. Yu, T. Sheng, H.-B. Ma, L.-N. Chen, M. Rauf, H.-P. Xia, Z.-Y. Zhou, S.-G. Sun, Constructing canopy-shaped molecular architectures to create local Pt surface sites with high tolerance to H₂S and CO for hydrogen electrooxidation, *Energy Environ. Sci.* 11 (2018) 166–171.
- [12] C. Jackson, L.F.J.M. Raymakers, M.J.J. Mulder, A.R.J. Kucernak, Assessing electrocatalyst hydrogen activity and CO tolerance: Comparison of performance obtained using the high mass transport ‘floating electrode’ technique and in electrochemical hydrogen pumps, *Appl. Catal., B* 268 (2020).
- [13] X. Yang, Y. Wang, X. Wang, B. Mei, E. Luo, Y. Li, Q. Meng, Z. Jin, Z. Jiang, C. Liu, J. Ge, W. Xing, CO-tolerant PEMFC anodes enabled by synergistic catalysis between iridium single-atom sites and nanoparticles, *Angew. Chem. Int. Ed.* 133 (2021) 26381–26387.
- [14] J. Zhang, X. Qu, L. Shen, G. Li, T. Zhang, J. Zheng, L. Ji, W. Yan, Y. Han, X. Cheng, Y. Jiang, S. Sun, Engineering the near-surface of PtRu₃ nanoparticles to improve hydrogen oxidation activity in alkaline electrolyte, *Small* 17 (2021), e2006698.
- [15] Y. Hu, J. Zhang, T. Shen, Y. Lu, K. Chen, Z. Tu, S. Lu, D. Wang, A low-temperature carbon encapsulation strategy for stable and poisoning-tolerant electrocatalysts, *Small Methods* 5 (2021), e2100937.
- [16] J.R. Varcoe, P. Atanassov, D.R. Dekel, A.M. Herring, M.A. Hickner, P.A. Kohl, A. R. Kucernak, W.E. Mustain, K. Nijmeijer, K. Scott, T. Xu, L. Zhuang, Anion-exchange membranes in electrochemical energy systems, *Energy Environ. Sci.* 7 (2014) 3135–3191.
- [17] B.P. Setzler, Z. Zhuang, J.A. Wittkopf, Y. Yan, Activity targets for nanostructured platinum-group-metal-free catalysts in hydroxide exchange membrane fuel cells, *Nat. Nanotechnol.* 11 (2016) 1020–1025.
- [18] D.R. Dekel, Review of cell performance in anion exchange membrane fuel cells, *J. Power Sources* 375 (2018) 158–169.

- [19] G. Huang, M. Mandal, X. Peng, A.C. Yang-Neyerlin, B.S. Pivovar, W.E. Mustain, P. A. Kohl, Composite poly(norbornene) anion conducting membranes for achieving durability, water management and high power (3.4 W/cm^2) in hydrogen/oxygen alkaline fuel cells, *J. Electrochem. Soc.* 166 (2019) F637–F644.
- [20] H.A. Miller, A. Lavacchi, F. Vizza, M. Marelli, F. Di Benedetto, F. D’Acapito, Y. Paska, M. Page, D.R. Dekel, A Pd/CeO₂ anode catalyst for high-performance platinum-free anion exchange membrane fuel cells, *Angew. Chem. Int. Ed.* 55 (2016) 6004–6007.
- [21] T.J. Omasta, X. Peng, H.A. Miller, F. Vizza, L. Wang, J.R. Varcoe, D.R. Dekel, W. E. Mustain, Beyond 1.0 W/cm^2 performance without platinum: The beginning of a new era in anion exchange membrane fuel cells, *J. Electrochem. Soc.* 165 (2018) J3039–J3044.
- [22] Y. Wang, Y. Yang, S. Jia, X. Wang, K. Lyu, Y. Peng, H. Zheng, X. Wei, H. Ren, L. Xiao, J. Wang, D.A. Muller, H.D. Abruna, B.J. Hwang, J. Lu, L. Zhuang, Synergistic Mn-Co catalyst outperforms Pt on high-rate oxygen reduction for alkaline polymer electrolyte fuel cells, *Nat. Commun.* 10 (2019) 1506.
- [23] H. Adabi, A. Shakouri, N. Ul Hassan, J.R. Varcoe, B. Zulevi, A. Serov, J. R. Regalbuto, W.E. Mustain, High-performing commercial Fe-N-C cathode electrocatalyst for anion-exchange membrane fuel cells, *Nat. Energy* 6 (2021) 834–843.
- [24] W. Sheng, H.A. Gasteiger, Y. Shao-Horn, Hydrogen oxidation and evolution reaction kinetics on platinum: Acid vs alkaline electrolytes, *J. Electrochem. Soc.* 157 (2010) B1529–B1536.
- [25] G. Zhao, J. Chen, W. Sun, H. Pan, Non-platinum group metal electrocatalysts toward efficient hydrogen oxidation reaction, *Adv. Funct. Mater.* 31 (2021) 2010633.
- [26] L. An, X. Zhao, T. Zhao, D. Wang, Atomic-level insight into reasonable design of metal-based catalysts for hydrogen oxidation in alkaline electrolytes, *Energy Environ. Sci.* 14 (2021) 2620–2638.
- [27] E.S. Davydova, S. Mukerjee, F. Jaouen, D.R. Dekel, Electrocatalysts for hydrogen oxidation reaction in alkaline electrolytes, *ACS Catal.* 8 (2018) 6665–6690.
- [28] S. Kim, Y.-E. Sung, Addressing a basic issue, *Nat. Energy* 6 (2021) 779–780.
- [29] S. Lu, J. Pan, A. Huang, L. Zhuang, J. Lu, Alkaline polymer electrolyte fuel cells completely free from noble metal catalysts, *Proc. Natl. Acad. Sci.* 105 (2008) 20611–20614.
- [30] T. Wang, M. Wang, H. Yang, M. Xu, C. Zuo, K. Feng, M. Xie, J. Deng, J. Zhong, W. Zhou, T. Cheng, Y. Li, Weakening hydrogen adsorption on nickel via interstitial nitrogen doping promotes bifunctional hydrogen electrocatalysis in alkaline solution, *Energy Environ. Sci.* 12 (2019) 3522–3529.
- [31] W. Ni, T. Wang, P.A. Schouwink, Y.C. Chuang, H.M. Chen, X. Hu, Efficient hydrogen oxidation catalyzed by strain-engineered nickel nanoparticles, *Angew. Chem. Int. Ed.* 59 (2020) 10797–10801.
- [32] L.X. Su, D. Gong, N. Yao, Y.B. Li, Z. Li, W. Luo, Modification of the intermediate binding energies on Ni/Ni₃N heterostructure for enhanced alkaline hydrogen oxidation reaction, *Adv. Funct. Mater.* 31 (2021).
- [33] S. Deng, X. Liu, X. Guo, T. Zhao, Y. Lu, J. Cheng, K. Chen, T. Shen, Y. Zhu, D. Wang, Insight into the hydrogen oxidation electrocatalytic performance enhancement on Ni via oxophilic regulation of MoO₂, *J. Energy Chem.* 54 (2021) 202–207.
- [34] A.G. Oshchepkov, G. Braesch, A. Bonnefond, E.R. Savinova, M. Chatenet, Recent advances in the understanding of nickel-based catalysts for the oxidation of hydrogen-containing fuels in alkaline media, *ACS Catal.* 10 (2020) 7043–7068.
- [35] J.-T. Ren, Y.-S. Wang, Y.-J. Song, L. Chen, Z.-Y. Yuan, Interface engineering of in-situ formed nickel hydr(oxy)oxides on nickel nitrides to boost alkaline hydrogen electrocatalysis, *Appl. Catal., B* 309 (2022), 121279.
- [36] J. Biemolt, J.C. Douglan, R.K. Singh, E.S. Davydova, N. Yan, G. Rothenberg, D. R. Dekel, An anion-exchange membrane fuel cell containing only abundant and affordable materials, *Energy Technol.* 9 (2021) 2000909.
- [37] W. Ni, T. Wang, F. Héroguel, A. Krammer, S. Lee, L. Yao, A. Schüller, J. S. Luterbacher, Y. Yan, X. Hu, An efficient nickel hydrogen oxidation catalyst for hydroxide exchange membrane fuel cells, *Nat. Mater.* 21 (2022) 804–810.
- [38] H.A. Firouzjaie, W.E. Mustain, Catalytic advantages, challenges, and priorities in alkaline membrane fuel cells, *ACS Catal.* 10 (2020) 225–234.
- [39] E.S. Davydova, F.D. Speck, M.T.Y. Paul, D.R. Dekel, S. Cherevko, Stability limits of Ni-based hydrogen oxidation electrocatalysts for anion exchange membrane fuel cells, *ACS Catal.* 9 (2019) 6837–6845.
- [40] F.D. Speck, F.S.M. Ali, M.T.Y. Paul, R.K. Singh, T. Böhm, A. Hofer, O. Kasian, S. Thiele, J. Bachmann, D.R. Dekel, T. Kallio, S. Cherevko, Improved hydrogen oxidation reaction activity and stability of buried metal-oxide electrocatalyst interfaces, *Chem. Mater.* 32 (2020) 7716–7724.
- [41] Y. Gao, H. Peng, Y. Wang, G. Wang, L. Xiao, J. Lu, L. Zhuang, Improving the antioxidation capability of the Ni catalyst by carbon shell coating for alkaline hydrogen oxidation reaction, *ACS Appl. Mater. Inter.* 12 (2020) 31575–31581.
- [42] J. Wang, X. Dong, J. Liu, W. Li, L.T. Roling, J. Xiao, L. Jiang, Ultrafine nickel nanoparticles encapsulated in N-doped carbon promoting hydrogen oxidation reaction in alkaline media, *ACS Catal.* 11 (2021) 7422–7428.
- [43] Y. Duan, Z.Y. Yu, L. Yang, L.R. Zheng, C.T. Zhang, X.T. Yang, F.Y. Gao, X.L. Zhang, X. Yu, R. Liu, H.H. Ding, C. Gu, X.S. Zheng, L. Shi, J. Jiang, J.F. Zhu, M.R. Gao, S. H. Yu, Bimetallic nickel-molybdenum/tungsten nanoalloys for high-efficiency hydrogen oxidation catalysis in alkaline electrolytes, *Nat. Commun.* 11 (2020) 4789.
- [44] Y. Yang, F.Y. Gao, X.L. Zhang, S. Qin, L.R. Zheng, Y.H. Wang, J. Liao, Q. Yang, M. R. Gao, Suppressing electron back-donation for a highly CO-tolerant fuel cell anode catalyst via cobalt modulation, *Angew. Chem. Int. Ed.* 61 (2022), e202208040.
- [45] S. Qin, Y. Duan, X.-L. Zhang, L.-R. Zheng, F.-Y. Gao, P.-P. Yang, Z.-Z. Niu, R. Liu, Y. Yang, X.-S. Zheng, J.-F. Zhu, M.-R. Gao, Ternary nickel–tungsten–copper alloy rivals platinum for catalyzing alkaline hydrogen oxidation, *Nat. Commun.* 12 (2021) 2686.
- [46] X. Zhao, X. Li, L. An, L. Zheng, J. Yang, D. Wang, Controlling the valence-electron arrangement of nickel active centers for efficient hydrogen oxidation electrocatalysis, *Angew. Chem. Int. Ed.* 61 (2022) e202206588.
- [47] Y. Men, X. Su, P. Li, Y. Tan, C. Ge, S. Jia, L. Li, J. Wang, G. Cheng, L. Zhuang, S. Chen, W. Luo, Oxygen-inserted top-surface layers of Ni for boosting alkaline hydrogen oxidation electrocatalysis, *J. Am. Chem. Soc.* 144 (2022) 12661–12672.
- [48] Y. Gao, Y. Yang, R. Schimmenti, E. Murray, H. Peng, Y. Wang, C. Ge, W. Jiang, G. Wang, F.J. DiSalvo, D.A. Muller, M. Mavrikakis, L. Xiao, H.D. Abruna, L. Zhuang, A completely precious metal-free alkaline fuel cell with enhanced performance using a carbon-coated nickel anode, *Proc. Natl. Acad. Sci. USA* 119 (2022) e2119883119.
- [49] C.J. Oluigbo, M. Xie, N. Ullah, S. Yang, W. Zhao, M. Zhang, X. Lv, Y. Xu, J. Xie, Novel one-step synthesis of nickel encapsulated carbon nanotubes as efficient electrocatalyst for hydrogen evolution reaction, *Int. J. Hydrol. Energy* 44 (2019) 2685–2693.
- [50] Y. Wu, X. Liu, D. Han, X. Song, L. Shi, Y. Song, S. Niu, Y. Xie, J. Cai, S. Wu, J. Kang, J. Zhou, Z. Chen, X. Zheng, X. Xiao, G. Wang, Electron density modulation of NiCo₂S₄ nanowires by nitrogen incorporation for highly efficient hydrogen evolution catalysis, *Nat. Commun.* 9 (2018) 1425.
- [51] J. Wang, Q. Zhao, H. Hou, Y. Wu, W. Yu, X. Ji, L. Shao, Nickel nanoparticles supported on nitrogen-doped honeycomb-like carbon frameworks for effective methanol oxidation, *RSC Adv.* 7 (2017) 14152–14158.
- [52] S.A.S. Machado, L.A. Avaca, The hydrogen evolution reaction on nickel surfaces stabilized by H-absorption, *Electrochim. Acta* 39 (1994) 1385–1391.
- [53] A.A. Philippov, A.M. Chibiryakov, I.P. Prosvirin, O.N. Martynov, Some like it weak: Different activity of Raney® nickel in transfer hydrogenation under air and inert atmosphere, *Appl. Catal., A* 605 (2020), 117788.
- [54] R.D. Kelley, G.A. Candela, T.E. Maday, D.E. Newbury, R.R. Schehl, Surface and bulk analysis of a deactivated raney nickel methanation catalyst, *J. Catal.* 80 (1983) 235–248.
- [55] X. Liu, L. Dai, Carbon-based metal-free catalysts, *Nat. Rev. Mater.* 1 (2016) 16064.
- [56] R. Paul, Q. Dai, C. Hu, L. Dai, Ten years of carbon-based metal-free electrocatalysts, *Carbon*, Energy 1 (2019) 19–31.
- [57] P.Z. Sun, Q. Yang, W.J. Kuang, Y.V. Stebunov, W.Q. Xiong, J. Yu, R.R. Nair, M. I. Katsnelson, S.J. Yuan, I.V. Grigorieva, M. Lozada-Hidalgo, F.C. Wang, A.K. Geim, Limits on gas impermeability of graphene, *Nature* 579 (2020) 229–232.
- [58] P.Z. Sun, M. Yagmurcukardes, R. Zhang, W.J. Kuang, M. Lozada-Hidalgo, B.L. Liu, H.M. Cheng, F.C. Wang, F.M. Peeters, I.V. Grigorieva, A.K. Geim, Exponentially selective molecular sieving through angstrom pores, *Nat. Commun.* 12 (2021) 7170.
- [59] S. Hu, M. Lozada-Hidalgo, F.C. Wang, A. Mishchenko, F. Schedin, R.R. Nair, E. W. Hill, D.W. Boukhvalov, M.I. Katsnelson, R.A. Dryfe, I.V. Grigorieva, H.A. Wu, A. K. Geim, Proton transport through one-atom-thick crystals, *Nature* 516 (2014) 227–230.
- [60] K. Hu, T. Ohto, Y. Nagata, M. Wakisaka, Y. Aoki, J.I. Fujita, Y. Ito, Catalytic activity of graphene-covered non-noble metals governed by proton penetration in electrochemical hydrogen evolution reaction, *Nat. Commun.* 12 (2021) 203.
- [61] N. Mehio, S. Dai, D.E. Jiang, Quantum mechanical basis for kinetic diameters of small gaseous molecules, *J. Phys. Chem. A* 118 (2014) 1150–1154.
- [62] E.R. Nightingale, Phenomenological theory of ion solvation. Effective radii of hydrated ions, *J. Phys. Chem.* 63 (1959) 1381–1387.
- [63] F.J. Luque, M. Orozco, P.K. Bhadane, S.R. Gadre, Effect of solvation on the shapes, sizes, and anisotropies of polyatomic anions via molecular electrostatic potential topography: an ab initio self-consistent reaction field approach, *J. Chem. Phys.* 100 (1994) 6718–6726.
- [64] M.D. Baer, C.J. Mundy, An ab initio approach to understanding the specific ion effect, *Faraday Discuss.* 160 (2013) 89–101.
- [65] H. Li, Z. Song, X. Zhang, Y. Huang, S. Li, Y. Mao, J. Ploehn Harry, Y. Bao, M. Yu, Ultrathin, molecular-sieving graphene oxide membranes for selective hydrogen separation, *Science* 342 (2013) 95–98.
- [66] Y. Tao, Q. Xue, Z. Liu, M. Shan, C. Ling, T. Wu, X. Li, Tunable hydrogen separation in porous graphene membrane: First-principle and molecular dynamic simulation, *ACS Appl. Mater. Inter.* 6 (2014) 8048–8058.
- [67] W. Kim Hyo, W. Yoon Hee, S.-M. Yoon, M. Yoo Byung, K. Ahn Byung, H. Cho Young, J. Shin Hye, H. Yang, U. Paik, S. Kwon, J.-Y. Choi, B. Park Ho, Selective gas transport through few-layered graphene and graphene oxide membranes, *Science* 342 (2013) 91–95.
- [68] Y. Fu, A.V. Rudnev, G.K.H. Wiberg, M. Arenz, Single graphene layer on Pt(111) creates confined electrochemical environment via selective ion transport, *Angew. Chem. Int. Ed.* 56 (2017) 12883–12887.
- [69] A. Cuesta, C. Gutiérrez, Study by fourier transform infrared spectroscopy of the adsorption of carbon monoxide on a nickel electrode at pH 3–14, *Langmuir* 14 (1998) 3397–3404.
- [70] S.-J. Huo, X.-K. Xue, Yan, Q.-X. Li, M. Ma, W.-B. Cai, Q.-J. Xu, M. Osawa, Extending in situ attenuated-total-reflection surface-enhanced infrared absorption spectroscopy to Ni, *Electrodes*, *J. Phys. Chem. B* 110 (2006) 4162–4169.
- [71] S. Zhu, T. Li, W.-B. Cai, M. Shao, CO₂ electrochemical reduction as probed through infrared spectroscopy, *ACS Energy Lett.* 4 (2019) 682–689.
- [72] R.J. Cvetanović, Y. Amenomiya, A temperature programmed desorption technique for investigation of practical catalysts, *Catal. Rev.* 6 (1972) 21–48.